# Relief of Tumor Hypoxia Using a Nanoenzyme Amplifies NIR-II Photoacoustic-Guided Photothermal Therapy

QIANG XUE,[1,2,†] SILUE ZENG,[2,3,†] YAGUANG REN,[2,†] YINGYING PAN,[2,4,†] JIANHAI CHEN,[2] NINGBO CHEN,[2,5] KENNETH K. Y. WONG,[5] LIANG SONG,[2] CHIHUA FANG,[3] JINHAN GUO,[1] JINFENG XU,[1] CHENGBO LIU,[2] JIE ZENG,[4] LITAO SUN,[6,7] HAI ZHANG,[1,8] AND JINGQIN CHEN[2,9]

[1]*Department of Ultrasound, Shenzhen People's Hospital, The Second Clinical College of Jinan University, The First Affiliated Hospital of Southern University of Science and Technology, Shenzhen 518020, China.*
[2]*Research Center for Biomedical Optics and Molecular Imaging, Key Laboratory of Biomedical Imaging Science and System, Shenzhen Institute of Advanced Technology, Chinese Academy of Sciences, Shenzhen 518055, China.*
[3]*Department of Hepatobiliary Surgery, Zhujiang Hospital, Southern Medical University, Guangzhou 510280, China.*
[4]*Department of Medical Ultrasonics, Third Affiliated Hospital of Sun Yat-Sen University, Guangzhou, China.*
[5] *The University of Hong Kong, Department of Electrical and Electronic Engineering, Hong Kong, China.*
[6]*Cancer Center, Department of Ultrasound Medicine, Zhejiang Provincial People's Hospital, Affiliated People's Hospital of Hangzhou Medical College, Hangzhou 310014, China.*
[7]*litaosun1971@sina.com*
[8]*szzhhans.scc.jnu@foxmail.com*
[9]*jq.chen@siat.ac.cn*
[†]*Contributed equally*

**Abstract:** Hypoxia is a critical tumor microenvironment (TME) component. It significantly impacts tumor growth and metastasis and is known to be a major obstacle for cancer therapy. Integrating hypoxia modulation with imaging-based monitoring represents a promising strategy that holds the potential for enhancing tumor theranostics. Herein, a kind of nanoenzyme Prussian blue (PB) is synthesized as a metal-organic framework (MOF) to load the second near-infrared (NIR-II) small molecule dye IR1061, which could catalyze hydrogen peroxide to produce oxygen and provide a photothermal conversion element for photoacoustic imaging (PAI) and photothermal therapy (PTT). To enhance stability and biocompatibility, silica was used as a coating for an integrated nanoplatform (SPI). SPI was found to relieve the hypoxic nature of the TME effectively, thus suppressing tumor cell migration and downregulating the expression of heat shock protein 70 (HSP70), both of which led to an amplified NIR-II PTT effect in vitro and in vivo, guided by the NIR-II PAI. Furthermore, label-free multi-spectral PAI permitted the real-time evaluation of SPI as a putative tumor treatment. A clinical histological analysis confirmed the amplified treatment effect. Hence, SPI combined with PAI could offer a new approach for tumor diagnosing, treating, and monitoring.

## 1. Introduction

The tumor microenvironment (TME) exhibits dynamic oxygen gradients and is often characterized by hypoxic regions resulting from oxygen consumption. This phenomenon is observed in nearly half of all solid tumors[1, 2]. A prolonged hypoxic environment significantly influences both the genomic and proteomic profiles of tumor cells[3]. Tumor cells can adapt and survive in hostile environments mediated by hypoxia. However, they are also stimulated to grow, invade, and metastasize, which represents a significant obstacle to cancer therapy[4, 5]. Multiple independent studies have consistently demonstrated that hypoxia is associated with a poorer prognosis in various types of cancer, such as ovarian, head and neck, prostate, and pancreatic cancer[6]. Breast cancer, the most prevalent malignancy among women globally, is frequently associated with the presence of hypoxic tumors and exhibits a low survival rate[7]. Breast cancer is characterized by aggressive growth, poor prognosis, high rates of recurrence, and early metastasis, particularly in the triple-negative breast cancer subtype[8]. Additionally, breast tumors were reported to have a notable degree of heterogeneity of hypoxia within each subtype[8, 9]. Therefore, modulating hypoxic TME in breast cancer could be a diagnostic and prognostic evaluation hallmark of the degree of malignancy and a specific target of tumor treatment.

In recent decades, researchers have made efforts to modulate the hypoxic condition using various strategies to attain enhanced therapeutic outcomes[4, 10]. For instance, it was reported that alleviating hypoxia could suppress multidrug resistance 1 gene expression, which encoded the P-gp protein. As a result, relieving hypoxia can enhance the efficacy of chemotherapy[11, 12]; facilitate oxygen supply to enhance radiotherapy[13, 14]; promote the generation of reactive oxygen species (ROS) to elevate the effectiveness of photodynamic and sonodynamic therapy[15-18]; as well as reduce immunosuppression and intrinsic resistance of tumor cells to immune system attacks, thus increasing the response rates of immunotherapy[19, 20]. The researchers noted that relieving tumor hypoxia promoted most existing tumor therapy modalities.

Photothermal therapy (PTT) is widely recognized as one of the most effective approaches for cancer treatment, which utilizes a laser to convert near-infrared (NIR) light into thermal energy and then selectively ablates local tumor cells[21-23]. However, it is essential to note that the necrosis induced by hyperthermia following PTT can trigger an excessive inflammatory response and activate tumor self-protection mechanisms, potentially leading to metastasis and recurrence[24, 25]. Heat shock proteins (HSPs) are critical molecular chaperones that play a significant role in cellular signal transduction and stress tolerance, particularly in response to heat stress[26, 27]. When exposed to heat stress, HSPs, particularly HSP70, are rapidly upregulated to facilitate the repair of thermally denatured proteins, thus promoting self-protection and contributing to thermoresistance in tumor cells[28, 29]. Leveraging this characteristic, strategies aimed at reducing the elevated expression of HSP70 during PTT hold great promise for enhancing the thermal sensitivity of tumor cells and promoting cell apoptosis[30, 31]. Hypoxia-inducible factor-1α (HIF-1α), a crucial regulator in hypoxic conditions, has been reported to be involved in the HSP70-mediated regulation of cell apoptosis[32, 33]. Therefore, we hypothesized that hypoxia is associated with the expression level of HSP70 in tumors and thus influences PTT effectiveness.

In this study, a kind of metal-organic framework (MOF), FDA-approved Prussian blue (PB), was synthesized as a nanoenzyme, mimicking the activities of peroxidase, catalase, and superoxide dismutase[34, 35]. Additionally, we loaded a second near-infrared (NIR-II) small molecule dye, IR1061, onto the platform as a photothermal element (Fig. 1). The NIR-II absorbance of IR1061 produced an efficient high photothermal conversion for PAI, enabled the evaluation of the in vivo behavior of SPI with high precision and accuracy. It was found that SPI could relieve the hypoxic TME, thus suppressing tumor cell migration and amplifying the PTT effect mediated by HSP 70 downregulation in vitro and in vivo[36-38]. PAI enabled the non-invasive in vivo detection of spatially resolved perfusion imaging of SPI and blood oxygenation within the TME. The proposed therapeutic effect was supported by histopathology.

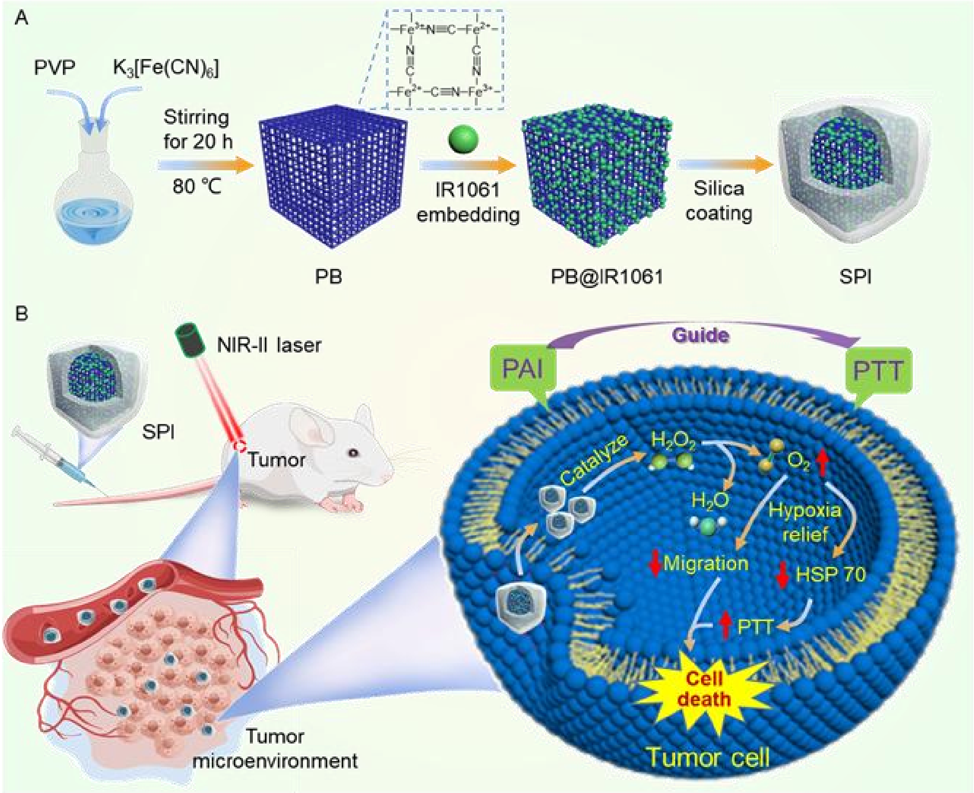

**Fig. 1.** Schematic illustration of (A) the preparation of $SiO_2$@PB-IR1061 (SPI) and (B) the mechanism by which relieving hypoxia of the tumor microenvironment amplifies NIR-II photoacoustic (PA) guided PTT.

## 2. Materials and Methods

### 2.1 Chemicals and materials

Potassium hexacyanoferrate ($K_3[Fe(CN)_6]$), polyvinylpyrrolidone K30 (PVP), tetraethylorthosilicate (TEOS), and hexadecyl trimethyl ammonium bromide (CTAB) were obtained from Aladdin Reagent Co., Ltd. (Shanghai, China). IR1061 dye and indocyanine green (ICG) were bought from Sigma-Aldrich (Darmstadt, Germany). Heat-inactivated fetal bovine serum (FBS) and Dulbecco's modified Eagle's medium (DMEM) were achieved from Thermo Fisher Scientific Co., Ltd. (Shanghai, China). A luminescent oxygen sensor ($[Ru(dpp)_3]Cl_2$) was bought from Mao Kang Biotechnology Co., Ltd. (Shanghai, China). 2-(4-Amidinophenyl)-6-indolecarbamidine dihydrochloride (DAPI), calcein-AM, propidium iodide (PI), a cell counting kit-8 (CCK-8), and an $H_2O_2$ detection kit were bought from Beyotime Biotechnology (Shanghai, China). The flow cytometry assay kit (Annexin V-FITC/PI) was provided by Yeasen (Shanghai, China).

### 2.2 Cell lines and animal model

Mouse breast tumor cell line 4T1, macrophage cell line RAW 264.7, and endothelial cell line HUVEC were provided by Shanghai Cell Bank, Chinese Academy of Sciences (CAS). They were cultured in DMEM containing 10% FBS and a 1% penicillin-streptomycin solution in a humidified incubator with 5% $CO_2$ at 37°C. Female BALB/c mice (4–6 weeks) were purchased from Baitantong Biotechnology Co., Ltd. (Zhuhai, China). Approximately $1\times10^6$ cells (in 50 μL of phosphate-buffered saline, PBS) were injected into the back of BALB/c mice for the subcutaneous breast cancer model. The investigators strictly followed the guidelines outlined in the "Guide for the Care and Use of Animals" issued by the Animal Care and Use Committee of Shenzhen Institute of Advanced Technology, Chinese Academy of Sciences (SIATACUC). All animal experiments were performed by the approved protocols of SIATACUC (SIAT-IACUC-210310-YGS-CJQ-A1784).

### *2.3 Synthesis and characterization of $SiO_2$@PB-IR1061 (SPI)*

Prussian blue (PB) was synthesized according to previous methods with modifications[39]. Briefly, $K_3[Fe(CN)_6]$ (453.4 mg) and PVP (6 g) were added to 80 mL of deionized water under magnetic stirring, and then 80 μL of concentrated hydrochloric acid was added. Afterwards, the mixture was heated at 80°C for 20 h in an oil bath and then was centrifuged at 11,000 rpm for 10 min. The precipitates were collected and subsequently washed three times with deionized water. The obtained PB was subjected to vacuum freeze-drying for 24 hours to obtain the final product. Next, the SPI nanoparticles were prepared as follows: CTAB (0.14 g) was dissolved in a mixture of ethanol (18 mL) and deionized water (3 mL) under vigorous stirring, producing a reaction media. PB (5 mg) and IR1061 (5 mg) were dissolved in deionized water (5 mL) and DMSO (5 mL), and then were transferred into the reaction media with slight stirring at 35 for 1 h. TEOS (300 μL) was added and reacted for 1 h at 35°C. SPI was obtained in precipitates by centrifugation (1100 rpm, 15 min) and several washes with methanol and deionized water solution, followed by vacuum drying to a powder for further use.

The morphology of PB and SPI was visualized using a transmission electron microscope (TEM) (FEI Talos F200X, 200 kV). Additionally, the elemental distribution of SPI was mapped using the same technique. We measured the size and zeta potential of the nanoparticle with the Zetasizer Nano-ZS (Malvern Instruments, USA). In order to detect the UV-vis-NIR spectrum, a UV-3600 spectrophotometer was used (SHIMADZU, Japan). Linear arrayed PAI system was also used for in vitro imaging studies.

### *2.4 Detection of oxygen production*

PBS, PB (50 μg/mL), and SPI (50 μg/mL) were suspended in a 5% $H_2O_2$ solution. An S4-Field kit dissolved oxygen meter (Mettler, Switzerland) was used to monitor the real-time oxygen concentration. An $H_2O_2$ detection kit was also used to detect the reductive concentration of $H_2O_2$. To further confirm the elevated oxygen concentration, an oxygen probe ($[Ru(dpp)_3]Cl_2$) was used to assess the production of oxygen according to the manufacturer's instructions.

### *2.5 Cell uptake of SPI*

To validate the distinct mechanisms of nanoparticle internalization into cells, fluorescence imaging was employed. SPI was labeled by ICG. Briefly, We added 1 mg of ICG powder to 5 mL of SPI solutions (2 mg/mL) and stirred for 12 hours at room temperature. Dialysis was then performed for 1 day against deionized water to remove unbound ICG, followed by centrifugation at 9000 g for 5 minutes to achieve SPI-ICG. Deionized water was used to re-disperse the hybrid for the ICG-labeled product, SPI-ICG. The procedures were conducted without the presence of direct light. To confirm ICG conjugation, the absorbance spectra of ICG-labeled SPI were measured with a UV-vis-NIR. After 24 h of cultivation in confocal dishes, 4T1 cells were further incubated with ICG and ICG-labeled SPI (0.1 mg/mL) for 4 h, respectively. PBS and ultrapure water were used to wash the redundant composites outside the cells three times. After that, the cells were fixed with a 4% paraformaldehyde solution for 10 min and DAPI (10 μg/mL) for 3 min, respectively. Fluorescence images of the stained cells were captured using a confocal laser scanning microscope (CLSM, Leica TCS SP5, Germany) with 405 nm and 638 nm excitation wavelengths for DAPI and ICG, respectively.

### *2.6 Photoacoustic (PA) properties of SPI*

To evaluate the PA properties of SPI, we performed PAI on samples at different concentrations (12.5, 25, 50, 100, and 200 µg/mL) at the wavelength of 1064 nm with the fluence of 15 mJ/cm$^2$. The mean of the maximum values of 250 measurements on each sample were calculated to analyze the relationship between the concentration of SPI and PA signal. Additionally, we irradiated the sample with around 1000 pulses and demonstrated the PA signal intensity of each irradiation to verify the stability of the SPI.

To further assess the effectiveness of the SPI, we created a phantom by injecting a nanoparticle solution (50 µg/mL) into plastic tubes and placing it at various depths within a chicken breast model. We then recorded a PA image of the cross-sectional area of the phantom using our PA imaging system.

### *2.7 Photothermal properties of SPI*

The photothermal experiments were conducted using a LWIRL1064-2W laser device (Laserwave, Beijing). Temperatures and thermal images were acquired every minute with a Fluke thermal imager. Aqueous solutions with varying concentrations of SPI (5, 10, 50, and 100 µg/mL) were exposed to a 1064 nm laser (0.7 W/cm$^2$) for 5 minutes. Additionally, a 1064 nm laser with different power densities (0.1, 0.3, 0.5, 0.7, and 1 W/cm$^2$) was employed to irradiate nanoparticle aqueous solutions (50 µg/mL) for 5 minutes each.

To evaluate the photothermal conversion efficiency (PCE) of SPI dispersions, the temperature changes over time were recorded under laser irradiation (1064 nm, 1 W/cm$^2$) until the sample reached a steady-state temperature. Subsequently, the laser was turned off, and the solution was allowed to return to ambient temperature. This process was repeated for five cycles to investigate SPI's photothermal stability (20 µg/mL).

### *2.8 In vitro PTT*

The cytotoxicity of PB and SPI was assessed using a CCK-8 assay. 4T1 cells, RAW264.7 cells, and HUVECs were cultured in a 96-well plate with complete culture medium ($5\times10^3$ cells per well) and incubated at 37°C for 24 hours. Subsequently, the cells were treated with different concentrations of nanoparticles in a fresh medium. After 24 hours of co-cultivation, 10 µL of CCK-8 reagent was added to each well and incubated for 30 minutes to 2 hours. The absorbance was measured using a microplate reader (BioTek Synergy 4, Winooski, VT), with untreated cells as controls.

In addition, a hemolysis test was conducted using red blood cells (RBCs) collected from mice. The RBCs were centrifuged at 1500 rpm for 3 minutes. The resulting pellet was mixed with SPI (10, 20, 50, 80, and 100 µg/mL) in a composite solution with a volume ratio of RBC/PBS = 1:9. The mixture was incubated at 37°C for 3 hours, followed by centrifugation at 10,000 rpm for 10 minutes. The supernatants of the suspensions were analyzed using UV-vis-NIR spectrometers at 541 nm. A PBS aqueous solution containing the same concentration of SPI was measured under similar conditions to determine the difference in absorption coefficient (DA). The hemolytic percentage (HP) was calculated by the equation: $HP\% = (DT-DA)/(DP-DA) \times 100\%$, where DT and DP represent the absorbances of the tested samples and the positive (deionized water) group, respectively[40, 41].

To evaluate the photothermal therapy (PTT) effects of SPI in vitro, 4T1 cells were seeded in 96-well plates at a density of $5\times10^3$ cells per well and incubated overnight. The cells were then divided into two groups: laser alone and SPI + laser. The cells in the SPI + laser group were first incubated with 50 µg/mL SPI for 12 hours, followed by laser irradiation for different durations (0, 0.5, 1, 3, 5, and 6 minutes) at a power density of 1 W/cm$^2$. After treatment, the cells were incubated for an additional 12 hours, and cytotoxicity was assessed using a CCK-8 assay following the manufacturer's instructions.

To further evaluate the cytotoxicity of the therapy, live and dead cell assays were performed. 4T1 cells were treated in the same manner as described above and co-stained with calcein AM and propidium iodide (PI) for 10 minutes according to the manufacturer's instructions. Fluorescence images of the cells were acquired using a confocal microscope. In addition, Annexin-FITC and PI assays were performed to assess the cytotoxicity of PTT by flow cytometry using a CytoFLEX instrument (Beckman, USA).

### *2.9 In vivo PA and fluorescence imaging of SPI*

Tumor-bearing mice were administered SPI (100 μL, 2 mg/mL) through intravenous injection (n = 3). In vivo, PA images were obtained at various time points (0, 1, 6, 9, 12, and 24 hours) using our custom-built PAI system mentioned in 2.6. An optical parametric oscillator (OPO) laser source (Innolas GmbH, Bonn, Germany) emitting pulsed lasers (8 ns, 30Hz) was coupled to an optical fiber (diameter: 1500 um) for the PA signal excitation. The generation of ultrasonic waves were recorded by a 128-element linear arrayed transducer (center frequency: 15 MHz, bandwidth: > 80%, Vernon). A 128-channel data acquisition systems (Vantage 128, Verasonics, Inc. US) synchronized with the excitation laser were used for photoacoustic data acquisition. The photoacoustic image can be observed in real time after data reconstruction using delay and sum method supplied by the data acquisition systems.

To compare the distribution of SPI and indocyanine green (ICG) in vivo, 4T1 tumor-bearing mice were randomly divided into two groups (n = 3 per group). They received intravenous injections of SPI and ICG at an equivalent dose of ICG (2 mg/kg). Fluorescent images were obtained using an in vivo fluorescence imaging system (IVIS Spectrum, PerkinElmer) at various time points (0, 1, 3, 6, 9, 12, and 24 hours). Furthermore, ex vivo fluorescence imaging was performed on mouse organs, including the heart, liver, spleen, lung, and kidney, 24 hours post-injection to examine the distribution of SPI and ICG in the organs.

### *2.10 In vivo PTT of SPI*

To investigate the photothermal therapy effect in vivo on tumor-bearing mice, subcutaneous 4T1 tumor-bearing mice were randomly assigned to six groups (n = 3 per group). The groups were as follows: (1) control group (treated with PBS); (2) laser irradiation alone; (3) SI group (administered with SI at a dose of 1 mg/kg); (4) SI group (administered with SI at a dose of 1 mg/kg) + laser irradiation; (5) SPI group (administered with SPI at a dose of 1 mg/kg); and (6) SPI group (administered with SPI at a dose of 1 mg/kg) + laser irradiation.

At 6 hours post-injection, laser irradiation was performed using a 1064 nm laser at a power density of 1 W/cm$^2$ for 5 minutes, and the temperature of the tumor was monitored using thermal imaging. Throughout the experiment, the mice's body weight and tumor volume were measured every two days to monitor their general health and tumor growth.

### *2.11 In vivo label-free multispectral PA imaging of blood oxygen saturation*

The custom-built PA imaging system was used to monitor the blood oxygen saturation ($sO_2$) information in the tumor through the multi-spectral PA method. Firstly, PA spectra of oxyhemoglobin ($HbO_2$) and deoxyhemoglobin (HHb) were measured by analyzing the multi-wavelength PA signal of arteries and veins in the mouse body prior to commencing the experiments[41]. Then 21 wavelengths ranging from 700 to 900 nm, with a step of 10 nm, were used to acquire the multi-spectral PA images of the tumor. Subsequently, we employed our own algorithm to extract the $HbO_2$ and HHb components from the multiple PA spectra of the tumor, and $sO_2$ was calculated according to the equation (1). 8 loops were applied for each recording to remove the system noise and other factors. Finally, we obtained the average $sO_2$ of the tumor under investigation.

$$sO_2 = HbO_2 / (HbO_2 + HHb) \qquad (1)$$

The average value of the $sO_2$ higher than 65% ($sO_2$ less than 65% is considered irrelevant or meaningless) within the tumor was calculated.

### *2.12 Western blot*

Total protein from 4T1 cells and tumor tissue was extracted using super RIPA lysis buffer (Thermo Fisher, USA) for Western blot analysis. The protein samples were resolved using SDS-PAGE and transferred onto PVDF membranes (Millipore). The membranes were then blocked with a wash buffer of 5% non-fat milk in Tris-buffered saline (TBS, Amresco, USA) containing 0.1% Tween-20, with gentle agitation for 1 hour at room temperature.

For primary antibody incubation, the following dilutions were used: HSP70 antibody (1:2000, AF1156, Beyotime) and β-actin antibody (1:2000, 30101ES60, Yeasen). The incubation was carried out overnight at 4°C with gentle agitation. Afterward, the membranes were washed thrice on a shaker for 10 minutes each.

Subsequently, the membranes were incubated with a 1:1000 dilution of goat anti-rabbit IgG (HRP) (1:2000, ab6721, Abcam) or anti-mouse IgG (HRP) (1:2000, ab6728, Abcam) for 1 hour. Following another three washes of 15 minutes each, the membranes were treated with an ECL detection reagent (Millipore) for 5 minutes before being exposed by a GelView 6000 Plus imaging system (China). The Western blot bands were quantified using ImageJ software to calculate the grey value (GV) of the protein bands. Data analysis was performed using the comparative GV method, and the expression levels were normalized to β-actin expression.

### *2.13 Biosafety evaluation*

At the end of the 16-day treatment period, all mice were euthanized. Tumors were carefully removed from the mice and photographed to observe the treatment outcome visually. Subsequently, the harvested tissues were fixed in 4% (v/v) paraformaldehyde overnight. The fixed tissues were then embedded in paraffin and sectioned at a thickness of 5 μm. These tissue sections were subjected to various staining techniques for histopathological evaluation. Hematoxylin and eosin (H&E) staining was performed to assess the overall tissue morphology and structural changes. Terminal-deoxynucleotidyl transferase-mediated nick end labeling (TUNEL) staining was used to detect apoptotic cells, while Ki67 staining was employed to evaluate cell proliferation. Images of the stained tissue slices were captured using an inverted optical microscope to visualize and analyze the histological features.

Additionally, to investigate the potential systemic effects of SPI, healthy BALB/c mice were intravenously injected with SPI at a dose of 20 mg/kg, with PBS serving as the control. After seven days of injection, approximately 1 mL of blood was collected from each animal via orbit blood withdrawal for blood panel analyses. Furthermore, the major organs, including the heart, liver, spleen, lungs, and kidneys, were harvested from each group of mice. These organs were fixed in 10% neutral buffered formalin, embedded in paraffin, and sectioned at a thickness of 5 μm. H&E staining was performed on the organ sections, and they were analyzed under a digital microscope to evaluate any potential organ-level effects or abnormalities.

### *2.14 Statistical analysis*

The data are achieved from triplicate experiments and presented as mean ± standard deviation (SD) in the figure legends. One-way ANOVA with Tukey's comparisons was used for multiple comparisons when more than two groups were compared, and the two-tailed

Student's t-test was used for two-group comparisons. All statistical tests were performed using GraphPad Prism software v. 8.0 (GraphPad Software). The differences between the test and control groups were considered to be significant at $*p < 0.05$ and very significant at $**p < 0.01$ and $***p < 0.001$.

## 3. Results and Discussion

### 3.1 Synthesis and characterization of $SiO_2$@PB-IR1061 (SPI)

To synthesize SPI, PB was first prepared by a reaction of $K_3[Fe(CN)_6]$ and polyvinylpyrrolidone (PVP) according to previous reports with some modifications[39]. NIR-II small molecule dye IR1061 was embedded into the metal organic frame of PB through the electrostatic adsorption effect. Then $SiO_2$ was coated onto the surface of PB-IR1061, producing SPI (Fig. 1). The TEM images show that PB was quadrate and homogeneous with an average diameter of about 100 nm, and after synthesizing to SPI (Fig. 2A and B), the diameter increased to about 150 nm, indicating successful coating with $SiO_2$ (Fig. 2C). As shown in the element maps of SPI, the Fe, N, and C elements clearly displayed inside the SPI nanoparticles, demonstrating the presence of PB; and the Si and O elements were on the shell (Fig. 2D), suggesting the existence of $SiO_2$ coating. The elements of SPI were further confirmed by energy-dispersive x-ray spectroscopy (EDX) analysis (Fig. 2E). Fig. 2F shows the zeta potential of PB and SPI, which were −38.37 mV and +32.03 mV, respectively. The change of the zeta potential from negative to positive was due to the surface coating of $SiO_2$. As a result of this change of zeta potential, it will be easy for SPI nanoparticles to enter tumor cells[35]. The UV-vis absorption spectrum of SPI displayed two intense peaks around 705 nm and 1064 nm, which were from PB (710 nm) and IR1061 (1061 nm) (Fig. 2G). According to the standard curve measured by ultraviolet spectrophotometer, the loading efficiency of SPI was 8.65% for IR1061[39]. These results demonstrated the successful synthesis of SPI. In addition, there was a good linear relationship between different concentrations and the absorbance at 1064 nm (Fig. 2H and Fig. S1). The average diameter and polymer dispersity index (PDI) of the SPI water solution showed no significant collapse for about two weeks (Fig. 2I). In the PBS and FBS solutions, SPI also displayed no apparent aggregation or change of absorbance intensity (Fig. S2 and S3). The temperature and pH of the physiological stability studies are 25.6 °C and 7.2. These results suggested that we have successfully synthesized SPI nanoplatform and solved the problem of hydrophobicity of IR1061. Therefore, it will be beneficial to in vitro and in vivo NIR-II PA imaging and PTT.

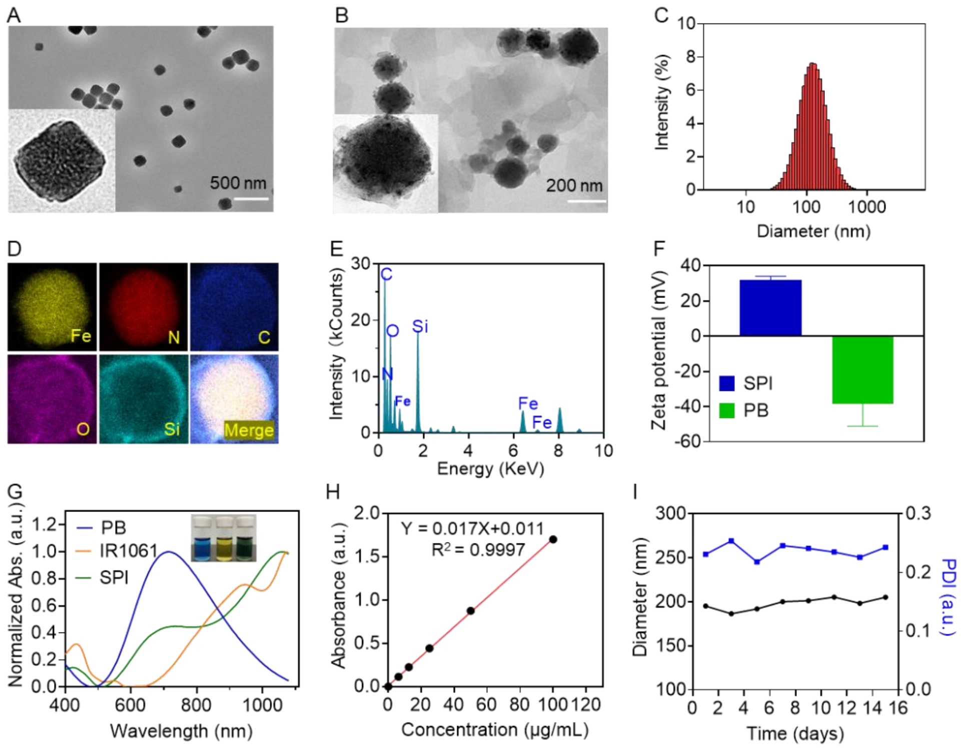

**Fig. 2.** Characterization of SPI. TEM images of (A) PB and (B) SPI. (C) The hydrodynamic sizes of SPI. (D) Elemental mapping images of SPI. (E) EDX analysis of SPI. (F) Zeta potentials of PB and SPI. (G) UV-vis absorbance spectra of PB, IR1061, and SPI. (H) The relationship between different concentrations of SPI and absorption. (I) The change in average diameter and polymer dispersity index (PDI) of SPI in an aqueous solution over 15 days.

### *3.2 NIR-II photoacoustic (PA) and photothermal properties of SPI*

Next, the photophysics properties of SPI were investigated. As shown in Fig. 3A, the photothermal conversion efficiency of SPI at 1064 nm wavelength was detected and calculated to be as high as 60.72%. However, the photothermal conversion efficiency of IR1061 under the same condition was 5.09% (Fig. S4). It was found that encapsulation in nanoconstruct could enhance the photothermal efficiency of IR1061 dye. The results showed that the photothermal efficiency of IR1061 was 5.09%, which was much less than that of SPI (60.72%), likely due to the heat led the aggregation of IR1061 and then induce the collapse of the NIR-II absorbance of IR1061. Excellent photothermal properties are essential for high-sensitive PA imaging and photothermal therapy (PTT), as these modalities are both based on the principle of heat generation by laser irradiation[42]. As expected, SPI showed very high PA sensitivity as even 10 μg/mL of such material can be clearly visualized under NIR-II pulsed laser irradiation (Fig. 3B). It is important to note that SPI exposed to around 1000 pulses of laser irradiation (15 mJ, 1064 nm) has no noticeable PA signal intensity loss, demonstrating its good PA stability (Fig. 3C). To evaluate the NIR-II PA imaging depth using SPI, a small plastic tube filled with the solution of SPI was embedded in the chicken breast and imaged by our custom-built PAI system[38]. As seen in Fig. 3D and E, the PA signal of SPI could still be detected at a depth of 4 cm, indicating that NIR-II PA imaging using SPI had high sensitivity and thus was beneficial for in vivo imaging. In addition, Fig. 3F–H shows that SPI has a dramatic concentration-dependent and laser power-dependent temperature elevation under 5 min of 1064 nm irradiation (Fig. 3I), indicating SPI has good photothermal stability in vitro. The peak temperature reached at approximately 60°C at a concentration as low as 50 μg/mL. These results demonstrated that SPI had excellent photothermal properties, which could serve as a suitable NIR-II PA imaging contrast and photothermal agent. It is also noteworthy that, as a result of the high photothermal conversion efficiency, we can use a small laser power for effective PTT treatment and reduce tissue damage.

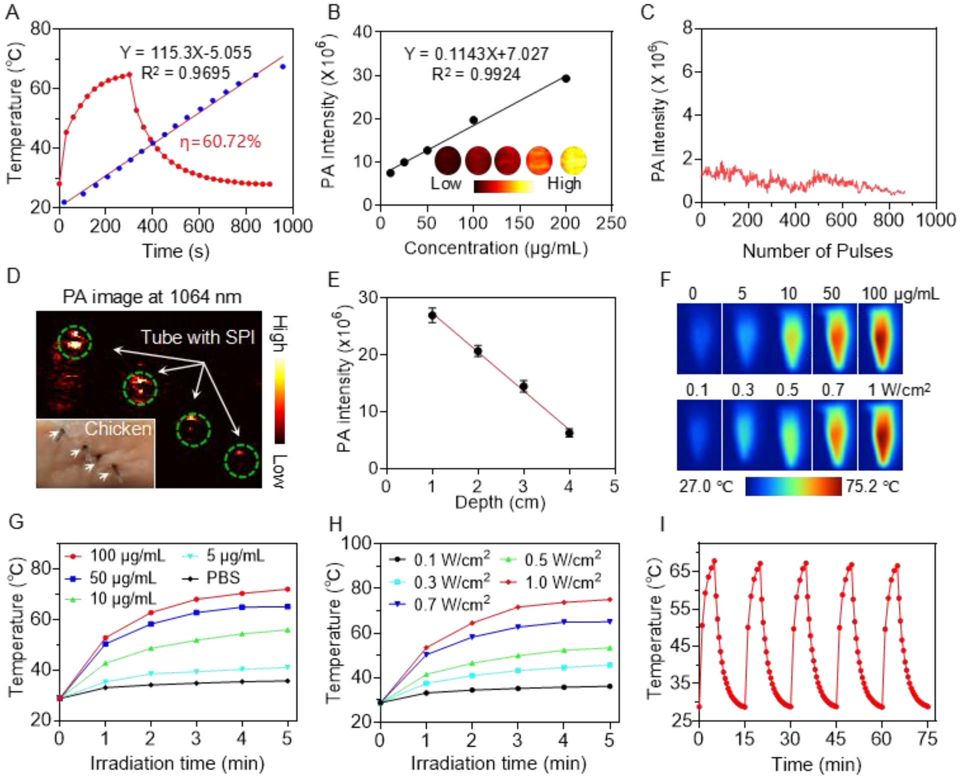

**Fig. 3.** NIR-II PA and photothermal properties of SPI. (A) Plot of cooling time versus the negative natural logarithm of the temperature driving force obtained from the cooling state, and the corresponding linear fitting curve. (B) PA signal of SPI with different concentrations. The inset is the corresponding PA images. (C) PA signal intensities upon irradiation with about 1000 pulses (1064 nm, 15 mJ/cm²). (D) PA signals of tubes with SPI at different depths in a chicken breast. (E) Relation between PA signal intensity and depth. (F) Thermal images of SPI at different concentrations and different power densities. (G) Temperature curves of SPI at different concentrations under 1064 nm laser irradiation (0.7 W/cm², 5 min). (H) Temperature curves of SPI (50 μg/mL) under 1064 nm laser irradiation at different power densities for 5 min. (I) Photothermal effects of SPI (50 μg/mL) with 1064 nm laser irradiation (1 W/cm²) after five irradiation-cooling cycles.

### *3.3 Catalase-like activity of SPI*

The chemical properties of SPI were also investigated. PB as a metal-organic framework (MOF) showed an excellent drug loading function and also has been reported as a nanoenzyme that displayed multienzyme-like activity, including that of peroxidase (POD), catalase (CAT), and superoxide dismutase (SOD)[34, 43]. We thus tested whether SPI promoted the conversion of $H_2O_2$ to oxygen. The catalase-like activity of SPI was first detected by a dissolved oxygen meter. As shown in Fig. 4A, massive bubbles were seen in PB- and SPI-treated $H_2O_2$ solutions in contrast to the PBS and $SiO_2$-IR1061 (SI) groups. The bubbles were further confirmed to be oxygen by a dissolved oxygen meter (Fig. 4B). The $H_2O_2$ concentration was also found to decrease in the PB- and SPI-treated groups (Fig. 4C).

The elevated oxygen concentration was also confirmed by the significantly reduced fluorescence of the oxygen probe ([Ru(dpp)$_3$]Cl$_2$) (Fig. 4D). Furthermore, we found that SPI, as well as PB, increased the oxygen production in 4T1 cells under hypoxic conditions, which mimicked the tumor microenvironment (Fig. 4E and F). These results were strongly evidenced by the consumption of $H_2O_2$ and the production of oxygen by SPI. In addition, it demonstrates that the modification of PB does not affect the functionality of nanoenzyme. As reported, elevated levels of reactive oxygen species (ROS), including $H_2O_2$ and hypoxia, are considered characteristic features of the tumor microenvironment. These factors are believed to play significant roles in the initiation and progression of tumor formation[2]. We thus hypothesized that SPI can increase oxygenation levels in the tumor microenvironment due to its catalase ability, which is beneficial for PTT.

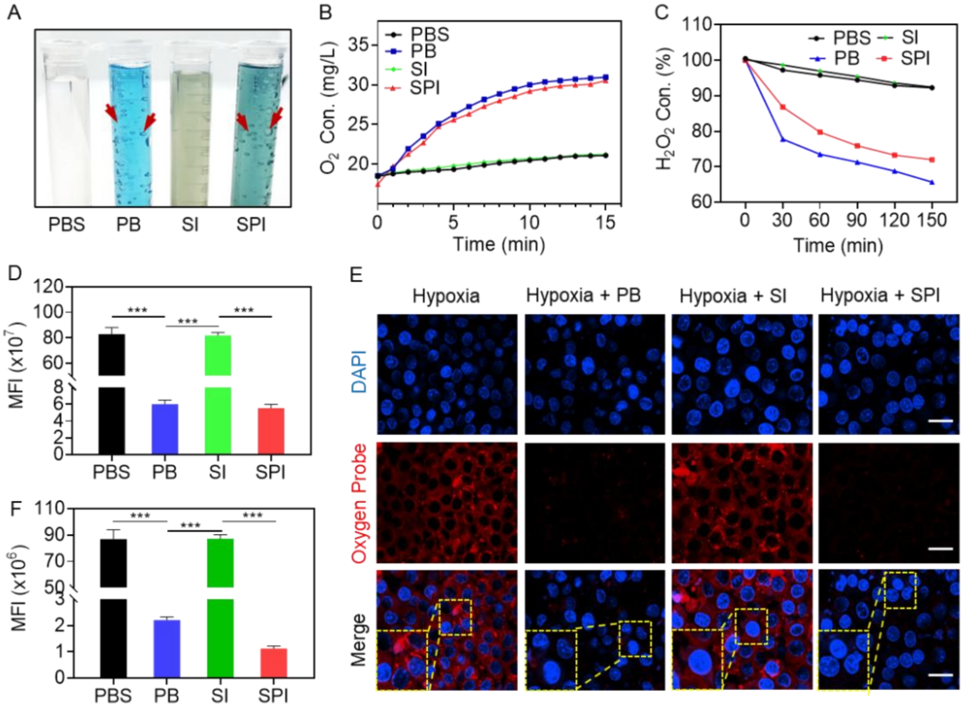

**Fig. 4.** Catalase-like properties of SPI. (A) The formation of gas bubbles in a 5% $H_2O_2$ solution; the yellow arrow represents bubbles. (B) Oxygen generation catalyzed by PBS, PB, SI, and SPI in an $H_2O_2$ solution as measured by the dissolved oxygen meter. (C) Concentration (Con.) of $H_2O_2$ after treatment with equal amounts of PBS, PB, and SPI. (D) Mean fluorescence intensity (MFI) of the oxygen probe [Ru(dpp)$_3$]Cl$_2$ after incubation with PBS, PB, SI, and SPI in a 5% $H_2O_2$ solution. (E) Fluorescence images showing the hypoxia level in 4T1 cells under hypoxic conditions with different treatments. Scale bar = 20 μm. (F) Quantitative fluorescence analysis of the hypoxia level in (E). The data are presented as mean ± standard deviation (SD). The error bar is derived from triplicate measurements. $***p < 0.001$, $**p < 0.01$, $*p < 0.05$.

### *3.4 In vitro amplified NIR-II PTT*

In order to evaluate the in vitro behavior of SPI, a small molecule dye, indocyanine green (ICG), was used to label SPI through physical binding. The absorbance and fluorescence spectra data confirmed the successful synthesis of ICG-labeled SPI (SPI-ICG) (Fig. S5A and B). 4T1 cells incubated with SPI-ICG exhibited stronger ICG fluorescence signals in the cytoplasm than those with free ICG (Fig. 5A and B), indicating SPI could enter 4T1 cells. The cytotoxicity of PB and SPI was determined using the CCK-8 assay. As shown in Fig. 5C and Fig. S6, PB and SPI at concentrations as high as 200 μg/mL displayed negligible cytotoxicity in 4T1, HUVEC, and RAW264.7 cells. When combined with NIR-II laser irradiation, the cytotoxicity of SPI on 4T1 cells showed a time-dependent increase (Fig. 5D). The cell live/dead staining assay and cell apoptosis assay confirmed the good in vitro PTT effect of SPI (Fig. 5E, F and G). It was worth noting that compared to SI + laser, SPI + laser showed an amplified PTT effect with a higher apoptosis rate (92.2%), potentially ascribing to the nanoenzyme activity of SPI. Therefore, these results demonstrated that SPI nanoparticles have good biosafety, can be easily devoured by tumor cells, and cause damage to them with the suitable laser irradiation.

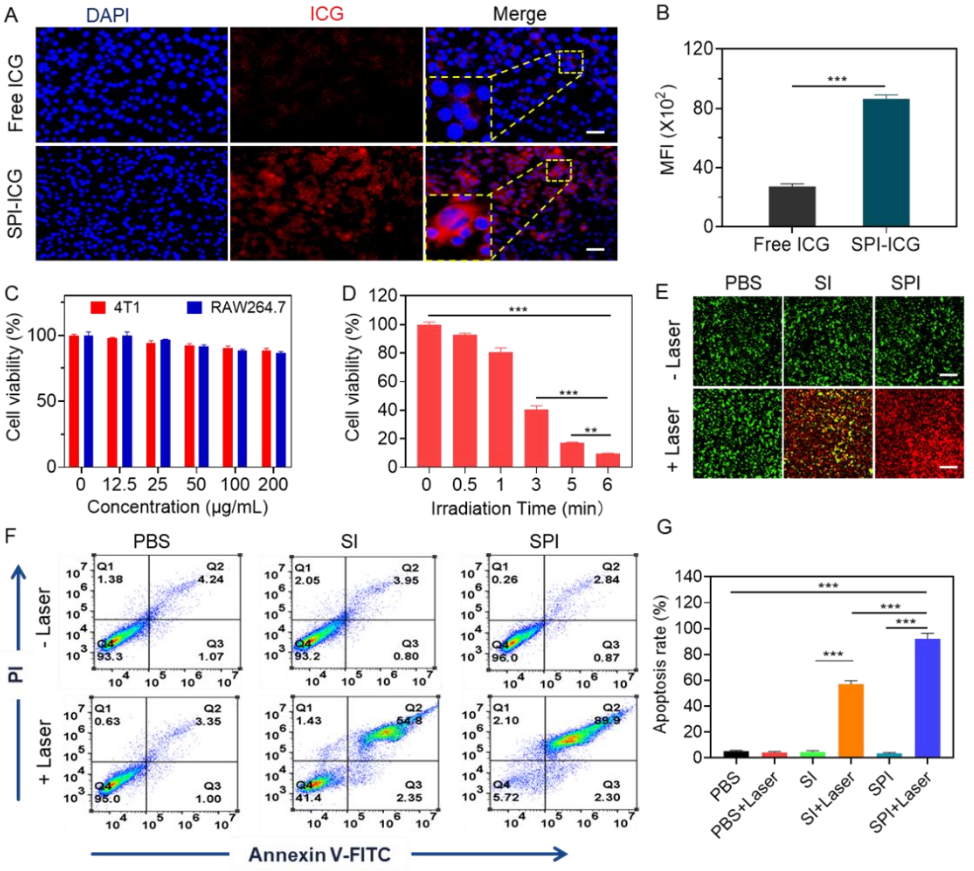

**Fig. 5.** Cellular uptake and PTT of SPI in vitro. (A and B) Confocal fluorescence images and corresponding mean fluorescence intensity (MFI) of 4T1 cells incubated with free ICG and ICG-labeled SPI for 4 h. Scale bar = 50 μm. (C) Viability of 4T1 cells and RAW264.7 cells treated with different concentrations of SPI. (D) Viability of 4T1 cells incubated with SPI (20 μg/mL) after irradiation for different time periods. (E) Confocal fluorescence images of 4T1 cells stained with calcein-AM/PI after incubation with various formulations. Green, calcein AM (live cells); red, PI (dead cells). Scale bar = 200 μm. (F) Apoptosis analysis of 4T1 cells treated with various formulations by flow cytometry. (G) Flow cytometry statistical analysis of apoptosis. The data are presented as mean ± standard deviation (SD). The error bar is derived from triplicate measurements. ***$p < 0.001$, **$p < 0.01$, *$p < 0.05$.

### *3.5 The influence of hypoxia relief on cell migration and PTT*

The mechanism of the amplified PTT effect was further investigated. As reported, hypoxia facilitated tumor cell migration, thus promoting tumor growth and metastasis[44]. Firstly, we designed a cell scratch assay to evaluate the influence of SPI on tumor cell migration (Fig. 6A). As shown in Fig. 6B and C, 4T1 cells treated with SPI in hypoxic condition had only a 25.9% migration rate, in contrast to the PBS and SI groups in which 4T1 cells had about a 50% migration rate under the same condition. This result was potentially ascribed to the fact that SPI catalyzed the overproduced $H_2O_2$ to oxygen and relieved hypoxic environment of the tumor, thus suppressing 4T1 cell migration. On the other hand, HSP70 is a molecular chaperone that facilitates correct protein folding and is expressed more abundantly under hyperthermia[45, 46]. This function of HSP70 renders tumor cells resistant to PTT[47]. We hypothesize that relief of the hypoxia perhaps inhibits the HSP70 expression and enhances the sensitivity of cell PTT. We found that 4T1 cells had low expression levels of HSP70. However, HSP70 was significantly upregulated in 4T1 cells that were treated by a combination of SI and 1064 nm laser irradiation for 5 min, indicating that PTT induced high expression of HSP70. Interestingly, under the same conditions, the HSP70 expression level was downregulated when the 4T1 cells were treated with SPI compared to treatment with SI (Fig. 6D and E), demonstrating that hypoxia relief by SPI indeed inhibited the expression of HSP70[48]. These results revealed that relieving hypoxia inhibited tumor cell migration and downregulated the expression of HSP70 (Fig. 6G), which amplified the PTT effect of SPI.

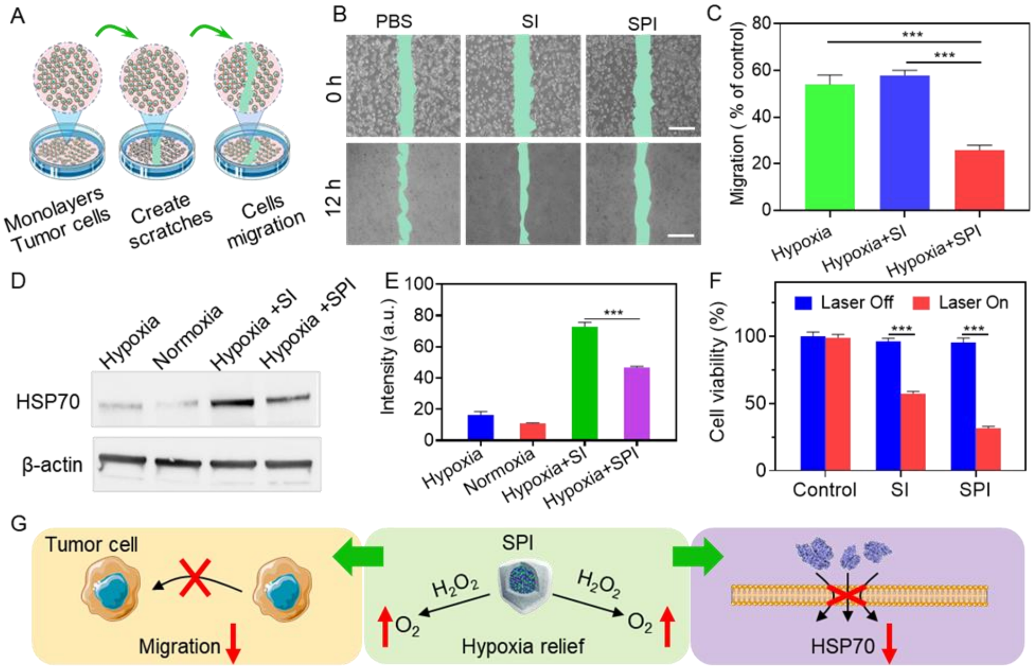

**Fig. 6.** The influence of hypoxia relief on cell migration and PTT. (A) The scheme of scratch assay. (B) Microscopic images and (C) percentage of 4T1 cell migration after 12 h incubationwith SI and SPI under hypoxia condition. Scale bar =500 μm. (D and E) Expression of HSP70 in 4T1 cells treated by hypoxia only, normoxia only, hypoxia + SI, and hypoxia + SPI under 1064 nm laser irradiation. (F) Viability of 4T1 cells treated with SI and SPI after laser irradiation for 5 min (1064 nm, 0.5 W/cm$^2$). (G) Schematic illustration of SPI relief of hypoxia and its application. The data are presented as mean ± standard deviation (SD). The error bar is derived from triplicate measurements. ***$p < 0.001$, **$p < 0.01$, *$p < 0.05$.

### *3.6 In vivo NIR-II PA imaging*

The in vivo performance of SPI was first analyzed by fluorescence imaging. As mentioned above, SPI was labeled by ICG to confer a fluorescence imaging ability. The loading ratio of ICG was 12.74%. In the 4T1 subcutaneous tumor-bearing mice model, SPI showed a higher fluorescence signal than free ICG in the tumor region, indicating SPI showed more accumulation in the tumor. With the increasing of time, SPI showed peak accumulation at 6 h post-injection and a gradual decrease over the next 18 h (Fig. 7A and B). This phenomenon can be attributed to the enhanced permeability and retention effect (EPR) commonly observed in solid tumors, contributing to the accumulation of SPI in the tumor microenvironment[49]. Major organs and tumors were harvested at 24 h post-injection. Ex vivo fluorescence images were shown in Fig. 7C and D. The tumors of mice treated with SPI had a visibly higher fluorescence signal than those injected with free ICG. Moreover, there were much more fluorescence signals in the liver and kidney, which indicated that SPI was mainly metabolized by the liver and kidney.

To overcome the limited penetration depth in fluorescence imaging, we turned to NIR-II PA imaging. PA imaging operates on the principle of "light in and ultrasound out," allowing for deeper tissue imaging in vivo[50, 51]. In Fig. 7E and F, we observed clear tumor cross-section structures on the ultrasound images (US, grey), and the PA signal at different depths exhibited higher intensity in the SPI group than in the free ICG group (Fig. S7A and B). This indicates the passive accumulation of SPI within the tumor. Notably, the peak time of accumulation observed in PA imaging was consistent with the results obtained from fluorescence imaging (Fig. 7G). These findings provide valuable insights into the in vivo behavior of SPI, which can serve as precise guidance for conducting in vivo PTT.

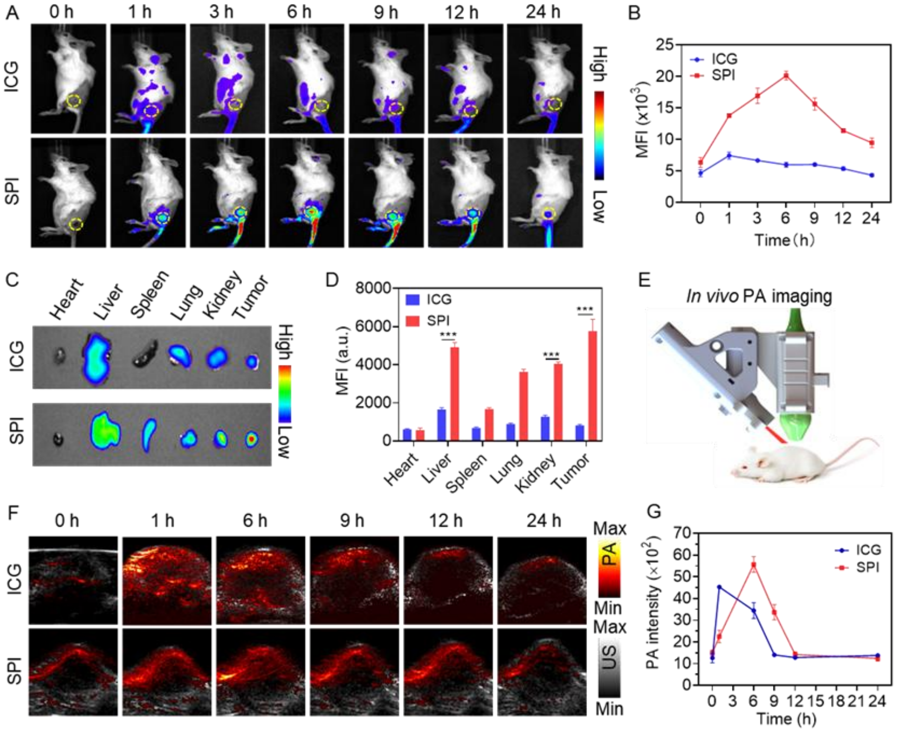

**Fig. 7.** In vivo fluorescence and PA imaging of SPI. (A) In vivo fluorescence images of subcutaneous 4T1 tumor-bearing mice at different time points after intravenous injection of free ICG and ICG labeled SPI, respectively. (B) Quantification of mean fluorescence intensity (MFI) of tumor areas in (A). (C) Ex vivo fluorescence images of major organs and tumors excised from mice at 24 h post-injection of ICG and ICG labeled SPI. (D) Quantitative biodistribution of ICG and ICG labeled SPI in major organs and tumors. (E) In vivo PA imaging probe. (F and G) In vivo PA images and quantification results of subcutaneous 4T1 tumor-bearing mice at different time points after intravenous injection of SPI and ICG, respectively. The data are presented as mean ± standard deviation (SD). The error bar is derived from triplicate measurements. ***$p < 0.001$, **$p < 0.01$, *$p < 0.05$.

### *3.7 In vivo amplified NIR-II PA-guided PTT*

The efficacy of SPI for treating tumors was investigated using a 4T1 subcutaneous tumor model. The treatment schedule was shown in Fig. 8A. Tumor-bearing mice were evenly distributed into six groups and treated as follows: PBS, PBS + laser, SI, SI + laser, SPI and SPI + laser. The tumor region was irradiated with an NIR-II laser (1064 nm, 5 min, 1W/cm$^2$) at 6 h post-intravenous injection. Fig. S8A and B show that the tumor temperature of the SPI + laser group reached 53.9 °C, the highest among the four groups. After about two weeks of treatment, the tumor size of the SPI + laser group decreased significantly compared with that of the other five groups (Fig. 8B and C), which could be verified by the pictures of tumor tissues dissected from sacrificed mice (Fig. S9).

Most importantly, a label-free multi-spectral PA imaging method was used to detect the $HbO_2$ and HHb in tumors to evaluate the hypoxia relief effect of SPI in vivo. As shown in Fig. 8D and E, the tumor displayed low blood oxygen saturation ($sO_2$) before treatment, a finding fully consistent with the hypoxic microenvironment proposed for 4T1 tumor tissue[52]. After 6 h of injection with SPI, the $sO_2$ increased from 69.4% to 74.02% , as can be seen in the PA parametric map of estimated $sO_2$ (n=3, Fig. 8D and Fig. S10). Based on these findings, and we can deduce that the presence of SPI in the tumor microenvironment led to an improvement in the hypoxic conditions within the tumor, presumably because SPI catalyzed the overexpressed $H_2O_2$ to oxygen and relieved the tumor hypoxic microenvironment. After two weeks of treatment, it can be seen by immunostaining that the expression levels of hypoxia-related HIF-1α and HSP70 proteins in the tumor tissue of SPI + laser groups were lower than those of the other five groups (Fig. 8F and Fig. S11), potentially demonstrating that the relieved hypoxic microenvironment by SPI downregulated the expression of HSP70 and thus enhanced the PTT effect of SPI.

The therapeutic effect of SPI was further confirmed by histopathological analyses. The tumor slices from the six groups were sectioned and stained with H&E, Ki67, and TUNEL (Fig. 8G, Fig. S12, S13 and S14). The results show that compared with the PBS, PBS + laser, SI, SI + laser, and SPI groups, the tumor in the SPI + laser treatment group displayed fewer proliferating malignant tumor cells and more apoptotic cells. Overall, the notable therapeutic efficacy observed with the combination of SPI and laser treatment can primarily be attributed to the catalase function exhibited by SPI that relieved the tumor hypoxic microenvironment and suppressed the expression of HSP70, thus amplifying the in vivo PTT effect.

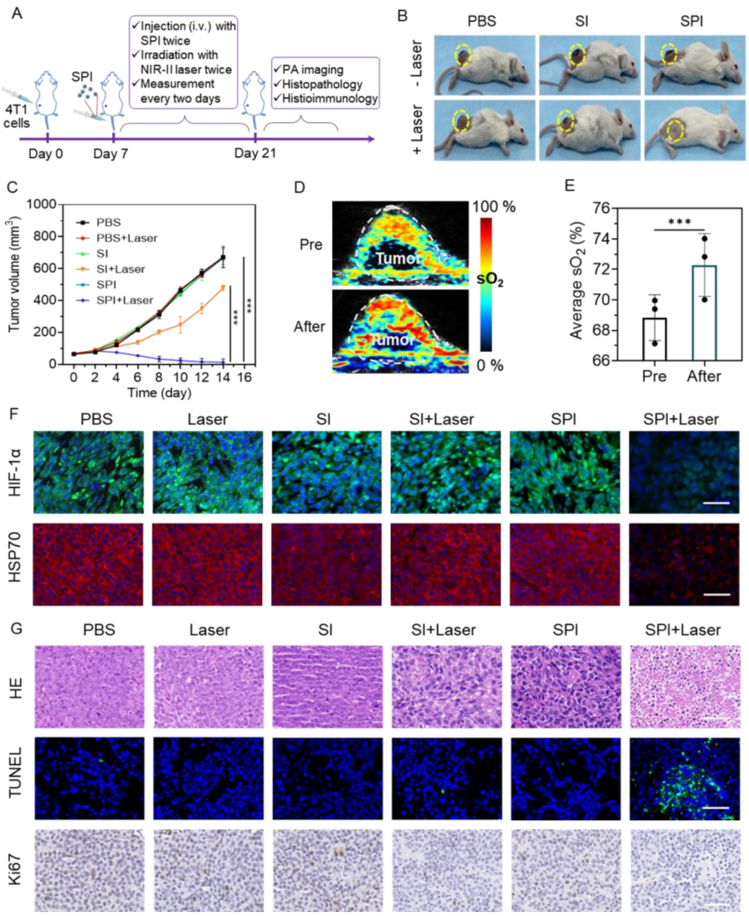

**Fig. 8.** PA-guided in vivo PTT. (A) In vivo PTT schedule. (B) Representative photographs of tumor-bearing mice treated by PBS, laser only, SI, SI + laser, SPI and SPI + laser. (C) The tumor volume change of tumor-bearing mice treated with PBS, laser only, SI, SI + laser, SPI and SPI + laser for 14 days of treatment. (D) Representative 2D PA images of solid tumors showing parametric map of estimated oxygen saturation ($sO_2$) before and after 6 h injection with SPI. (E) Relative quantification of oxygen saturation in the tumor areas in (D). (F) Representative immunofluorescence images of HIF-1α and HSP70 in the tumor tissue from tumor-bearing mice treated by PBS, laser only, SI, SI + Laser, SPI and SPI + laser. Scale bar = 100 μm. (G) Representative HE, Ki67, Tunnel staining images of the tumor tissue from tumor-bearing mice treated by PBS, laser only, SI, SI + laser, SPI and SPI + laser. Scale bar = 100 μm. The data are presented as mean ± standard deviation (SD). The error bar is derived from triplicate measurements. $^{***}p < 0.001$, $^{**}p < 0.01$, $^{*}p < 0.05$.

### *3.8 Biosafety evaluation*

To assess the biosafety of SPI for potential clinical use, comprehensive investigations were conducted both in vitro and in vivo. Fig. S15 demonstrates that throughout the 16-day treatment, there was no significant loss in body weight, indicating that the injection of SPI and NIR-II laser irradiation did not affect the mice's diet. Furthermore, a hemolysis test showed that after a three-hour incubation of red blood cells with SPI, there was no noticeable hemolysis, with hemolysis levels remaining below 5% (Fig. S16), indicating excellent blood compatibility of SPI. Moreover, when healthy mice were treated with SPI for seven consecutive days, no tissue damage or inflammatory lesions were observed in any major organs, including the heart, liver, spleen, lung, and kidney (Fig. S17). Additionally, blood analysis revealed no significant differences between SPI-treated mice and healthy mice (Fig. S18), further confirming the favorable in vitro and in vivo biocompatibility of SPI.

Collectively, these findings support the conclusion that SPI exhibits good biosafety profiles, making it a promising candidate for clinical applications.

## 4. Conclusion

In summary, we demonstrated a new anticancer strategy that relief of tumor hypoxia using a nanoenzyme amplified NIR-II PA-guided photothermal therapy. The integrated therapy nanoplatform SPI was developed by coating PB and IR1061 with $SiO_2$ and showed good stability and biocompatibility. PB has been shown to have catalase activity and to be capable of promoting hydrogen peroxide dismutation with subsequent oxygen production, allowing SPI to relieve the hypoxia of the TME and further downregulate the expression of HIF-1α and HSP70 in vitro and in vivo. IR1061 possessed a high photothermal conversion efficiency, allowing NIR-II PA imaging to be utilized for the in vivo tracking of SPI. Both PA imaging and fluorescence imaging techniques demonstrated the effective tumor targeting ability of SPI, in vitro experiments, and in vivo studies. Moreover, based on label-free PA imaging and histopathology analysis, SPI was found to suppress tumor cell migration and significantly enhance NIR-II PTT therapeutic effect, including hypoxia inhibition and apoptosis-mediated anticancer activity. Moreover, SPI exhibited excellent biosafety profiles both in vitro and in vivo. These results demonstrated that SPI possesses high potential for utilization in NIR-II PA imaging-guided tumor therapy.

**Funding.** This work was supported by National Key Research and Development Program of China (2021YFE0202200, 2022YFE0132300, 2020YFA0908800); National Natural Science Foundation of China (NSFC) Grant (82172008, 82122034, 92059108, 81927807); Chinese Academy of Sciences Grant (Youth Innovation Promotion Association 2019352, 2023374; GJJSTD20210003); CAS Key Laboratory of Health Informatics (2011DP173015); Shenzhen Science and Technology Innovation Grant (JCYJ20220818101403008, JCYJ20190806150001764, JCYJ20180228164437735); Guangdong Provincial Key Laboratory of Biomedical Optical Imaging (2020B121201010); Shenzhen Key Laboratory for Molecular Imaging (ZDSY20130401165820357). Guangdong Basic and Applied Basic Research Foundation (2020A1515010978).

**Disclosures.** The authors declare no conflicts of interest.

**Data availability.** All relevant data are available from the corresponding author upon request.

**Supplemental document.** See Supplement 1 for supporting content.

## References

1. W. R. Wilson, and M. P. Hay, "Targeting hypoxia in cancer therapy," Nat Rev Cancer **11**, 393-410 (2011).
2. A. L. Harris, "Hypoxia--a key regulatory factor in tumour growth," Nat Rev Cancer **2**, 38-47 (2002).
3. N. Dhani, A. Fyles, D. Hedley, and M. Milosevic, "The clinical significance of hypoxia in human cancers," Semin Nucl Med **45**, 110-121 (2015).
4. A. Sahu, I. Kwon, and G. Tae, "Improving cancer therapy through the nanomaterials-assisted alleviation of hypoxia," Biomaterials **228**, 119578 (2020).
5. A. Sahu, W. I. Choi, and G. Tae, "Recent Progress in the Design of Hypoxia-Specific Nano Drug Delivery Systems for Cancer Therapy," Advanced Therapeutics **1** (2018).
6. G. L. Semenza, "Hypoxia-inducible factors: mediators of cancer progression and targets for cancer therapy," Trends Pharmacol Sci **33**, 207-214 (2012).
7. H. Sung, J. Ferlay, R. L. Siegel, M. Laversanne, I. Soerjomataram, A. Jemal, and F. Bray, "Global Cancer Statistics 2020: GLOBOCAN Estimates of Incidence and Mortality Worldwide for 36 Cancers in 185 Countries," CA Cancer J Clin **71**, 209-249 (2021).
8. W. D. Foulkes, I. E. Smith, and J. S. Reis-Filho, "Triple-negative breast cancer," N Engl J Med **363**, 1938-1948 (2010).
9. C. C. Wong, D. M. Gilkes, H. Zhang, J. Chen, H. Wei, P. Chaturvedi, S. I. Fraley, C. M. Wong, U. S. Khoo, I. O. Ng, D. Wirtz, and G. L. Semenza, "Hypoxia-inducible factor 1 is a master regulator of breast cancer metastatic niche formation," Proc Natl Acad Sci U S A **108**, 16369-16374 (2011).
10. J. J. Liu, Q. Chen, L. Z. Feng, and Z. Liu, "Nanomedicine for tumor microenvironment modulation and cancer treatment enhancement," Nano Today **21**, 55-73 (2018).
11. D. Samanta, D. M. Gilkes, P. Chaturvedi, L. Xiang, and G. L. Semenza, "Hypoxia-inducible factors are required for chemotherapy resistance of breast cancer stem cells," Proc Natl Acad Sci U S A **111**, E5429-5438 (2014).

12. X. Huang, J. Zhuang, S. W. Chung, B. Huang, G. Halpert, K. Negron, X. Sun, J. Yang, Y. Oh, P. M. Hwang, J. Hanes, and J. S. Suk, "Hypoxia-tropic Protein Nanocages for Modulation of Tumor- and Chemotherapy-Associated Hypoxia," ACS Nano **13**, 236-247 (2019).
13. M. R. Horsman, L. S. Mortensen, J. B. Petersen, M. Busk, and J. Overgaard, "Imaging hypoxia to improve radiotherapy outcome," Nat Rev Clin Oncol **9**, 674-687 (2012).
14. M. W. Dewhirst, Y. Cao, and B. Moeller, "Cycling hypoxia and free radicals regulate angiogenesis and radiotherapy response," Nat Rev Cancer **8**, 425-437 (2008).
15. X. Li, N. Kwon, T. Guo, Z. Liu, and J. Yoon, "Innovative Strategies for Hypoxic-Tumor Photodynamic Therapy," Angew Chem Int Ed Engl **57**, 11522-11531 (2018).
16. B. Pucelik, A. Sułek, A. Barzowska, and J. M. Dąbrowski, "Recent advances in strategies for overcoming hypoxia in photodynamic therapy of cancer," Cancer Lett **492**, 116-135 (2020).
17. K. Yang, L. Yue, G. Yu, L. Rao, R. Tian, J. Wei, Z. Yang, C. Sun, X. Zhang, M. Xu, Z. Yuan, X. Chen, and R. Wang, "A hypoxia responsive nanoassembly for tumor specific oxygenation and enhanced sonodynamic therapy," Biomaterials **275**, 120822 (2021).
18. C. McEwan, J. Owen, E. Stride, C. Fowley, H. Nesbitt, D. Cochrane, C. C. Coussios, M. Borden, N. Nomikou, A. P. McHale, and J. F. Callan, "Oxygen carrying microbubbles for enhanced sonodynamic therapy of hypoxic tumours," J Control Release **203**, 51-56 (2015).
19. G. Lan, K. Ni, Z. Xu, S. S. Veroneau, Y. Song, and W. Lin, "Nanoscale Metal-Organic Framework Overcomes Hypoxia for Photodynamic Therapy Primed Cancer Immunotherapy," J Am Chem Soc **140**, 5670-5673 (2018).
20. Y. Zhang, Y. Liao, Q. Tang, J. Lin, and P. Huang, "Biomimetic Nanoemulsion for Synergistic Photodynamic-Immunotherapy Against Hypoxic Breast Tumor," Angew Chem Int Ed Engl **60**, 10647-10653 (2021).
21. J. Zhou, M. Li, Y. Hou, Z. Luo, Q. Chen, H. Cao, R. Huo, C. Xue, L. Sutrisno, L. Hao, Y. Cao, H. Ran, L. Lu, K. Li, and K. Cai, "Engineering of a Nanosized Biocatalyst for Combined Tumor Starvation and Low-Temperature Photothermal Therapy," ACS Nano **12**, 2858-2872 (2018).
22. Y. Zhao, T. Zhao, Y. Cao, J. Sun, Q. Zhou, H. Chen, S. Guo, Y. Wang, Y. Zhen, X. J. Liang, and S. Zhang, "Temperature-Sensitive Lipid-Coated Carbon Nanotubes for Synergistic Photothermal Therapy and Gene Therapy," ACS Nano **15**, 6517-6529 (2021).
23. N. S. H. Motlagh, P. Parvin, Z. H. Mirzaie, R. Karimi, J. H. Sanderson, and F. Atyabi, "Synergistic performance of triggered drug release and photothermal therapy of MCF7 cells based on laser activated PEGylated GO + DOX," Biomed. Opt. Express 11, 3783-3794 (2020).
24. L. Li, X. Liang, T. He, X. Li, X. Huang, N. Wang, M. Shen, Y. Shu, R. Wu, M. Zhang, Q. Wu, and C. Gong, "Multifunctional light-activatable nanocomplex conducting temperate-heat photothermal therapy to avert excessive inflammation and trigger augmented immunotherapy," Biomaterials **290**, 121815 (2022).
25. X. Li, Y. Pan, C. Chen, Y. Gao, X. Liu, K. Yang, X. Luan, D. Zhou, F. Zeng, X. Han, and Y. Song, "Hypoxia-Responsive Gene Editing to Reduce Tumor Thermal Tolerance for Mild-Photothermal Therapy," Angew Chem Int Ed Engl **60**, 21200-21204 (2021).
26. H. M. Beere, and D. R. Green, "Stress management - heat shock protein-70 and the regulation of apoptosis," Trends Cell Biol **11**, 6-10 (2001).
27. R. Suto, and P. K. Srivastava, "A mechanism for the specific immunogenicity of heat shock protein-chaperoned peptides," Science **269**, 1585-1588 (1995).
28. Y. Zhou, B. Niu, Y. Zhao, J. Fu, T. Wen, K. Liao, G. Quan, X. Pan, and C. Wu, "Multifunctional nanoreactors-integrated microneedles for cascade reaction-enhanced cancer therapy," J Control Release **339**, 335-349 (2021).
29. J. S. Ni, X. Zhang, G. Yang, T. Kang, X. Lin, M. Zha, Y. Li, L. Wang, and K. Li, "A Photoinduced Nonadiabatic Decay-Guided Molecular Motor Triggers Effective Photothermal Conversion for Cancer Therapy," Angew Chem Int Ed Engl **59**, 11298-11302 (2020).
30. M. Y. Sherman, and V. L. Gabai, "Hsp70 in cancer: back to the future," Oncogene **34**, 4153-4161 (2015).
31. L. F. Yang, C. C. Ren, M. Xu, Y. L. Song, Q. L. Lu, Y. L. Wang, Y. Zhu, X. X. Wang, and N. Li, "Rod-shape inorganic biomimetic mutual-reinforcing $MnO_2$-Au nanozymes for catalysis-enhanced hypoxic tumor therapy," Nano Research **13**, 2246-2258 (2020).
32. J. Cao, L. Yang, L. Wang, Q. Zhao, D. Wu, M. Li, and Y. Mu, "Heat shock protein 70 attenuates hypoxia-induced apoptosis of pulmonary microvascular endothelial cells isolated from neonatal rats," Mol Med Rep **24** (2021).
33. S. Chen, and N. Sang, "Hypoxia-Inducible Factor-1: A Critical Player in the Survival Strategy of Stressed Cells," J Cell Biochem **117**, 267-278 (2016).
34. W. Zhang, S. Hu, J. J. Yin, W. He, W. Lu, M. Ma, N. Gu, and Y. Zhang, "Prussian Blue Nanoparticles as Multienzyme Mimetics and Reactive Oxygen Species Scavengers," J Am Chem Soc **138**, 5860-5865 (2016).
35. X. Cai, W. Gao, M. Ma, M. Wu, L. Zhang, Y. Zheng, H. Chen, and J. Shi, "A Prussian Blue-Based Core-Shell Hollow-Structured Mesoporous Nanoparticle as a Smart Theranostic Agent with Ultrahigh pH-Responsive Longitudinal Relaxivity," Adv Mater **27**, 6382-6389 (2015).
36. M. Li, Y. Tang, and J. Yao, "Photoacoustic tomography of blood oxygenation: A mini review," Photoacoustics **10**, 65-73 (2018).
37. Y. Wang, S. Hu, K. Maslov, Y. Zhang, Y. Xia, and L. V. Wang, "In vivo integrated photoacoustic and confocal microscopy of hemoglobin oxygen saturation and oxygen partial pressure," Opt Lett **36**, 1029-1031 (2011).

38. R. Gao, F. Liu, W. Liu, S. Zeng, J. Chen, R. Gao, L. Wang, C. Fang, L. Song, A. C. Sedgwick, J. L. Sessler, J. Chu, F. Yan, and C. Liu, "Background-suppressed tumor-targeted photoacoustic imaging using bacterial carriers," Proc Natl Acad Sci U S A **119** (2022).
39. J. J. Hu, Y. Chen, Z. H. Li, S. Y. Peng, Y. Sun, and X. Z. Zhang, "Augment of Oxidative Damage with Enhanced Photodynamic Process and MTH1 Inhibition for Tumor Therapy," Nano Lett **19**, 5568-5576 (2019).
40. G. Xu, X. Bao, J. Chen, B. Zhang, D. Li, D. Zhou, X. Wang, C. Liu, Y. Wang, and S. Qu, "In Vivo Tumor Photoacoustic Imaging and Photothermal Therapy Based on Supra-(Carbon Nanodots)," Adv Healthc Mater **8**, e1800995 (2019).
41. J. Chen, S. Zeng, Q. Xue, Y. Hong, L. Liu, L. Song, C. Fang, H. Zhang, B. Wang, A. C. Sedgwick, P. Zhang, J. L. Sessler, C. Liu, and J. Chen, "Photoacoustic image-guided biomimetic nanoparticles targeting rheumatoid arthritis," Proc Natl Acad Sci U S A **119**, e2213373119 (2022).
42. Z. Z. Qin, Y. Liu, J. K. Chi, Y. M. Ma, and M. J. Sun, "The sparse array elements selection in sparse imaging of circular-array photoacoustic tomography," Journal of Innovative Optical Health Sciences **15** (2022).
43. C. Sahlgren, M. V. Gustafsson, S. Jin, L. Poellinger, and U. Lendahl, "Notch signaling mediates hypoxia-induced tumor cell migration and invasion," Proc Natl Acad Sci U S A **105**, 6392-6397 (2008).
44. J. Y. Zhao, F. Gong, N. L. Yang, H. L. Lei, Z. H. Han, Y. Q. Yang, and L. Cheng, "$H_2O_2$-sensitive nanoscale coordination polymers for photoacoustic tumors imaging via in vivo chromogenic assay," Journal of Innovative Optical Health Sciences **15** (2022).
45. Y. Xi, X. Xie, Y. Peng, P. Liu, J. Ding, and W. Zhou, "DNAzyme-adsorbed polydopamine@MnO(2) core-shell nanocomposites for enhanced photothermal therapy via the self-activated suppression of heat shock protein 70," Nanoscale **13**, 5125-5135 (2021).
46. B. Zhang, C. W. Shao, K. M. Zhou, Q. Li, Y. T. Duan, Y. S. Yang, and H. L. Zhu, "A NIR-triggered multifunctional nanoplatform mediated by Hsp70 siRNA for chemo-hypothermal photothermal synergistic therapy," Biomater Sci **9**, 6501-6509 (2021).
47. X. Shu, Y. Chen, P. Yan, Y. Xiang, Q. Y. Shi, T. Yin, P. Wang, L. H. Liu, and X. Shuai, "Biomimetic nanoparticles for effective mild temperature photothermal therapy and multimodal imaging," J Control Release **347**, 270-281 (2022).
48. L. Meng, X. Ma, S. Jiang, S. Zhang, Z. Wu, B. Xu, Z. Lei, L. Liu, and W. Tian, "Twisted Intramolecular Charge Transfer—Aggregation-Induced Emission Fluorogen with Polymer Encapsulation-Enhanced Near-Infrared Emission for Bioimaging," CCS Chemistry **3**, 2084-2094 (2021).
49. J. Xia, M. A. Lediju Bell, J. Laufer, and J. Yao, "Translational Photoacoustic Imaging for Disease Diagnosis, Monitoring, and Surgical Guidance: introduction to the feature issue," Biomed. Opt. Express 12, 4115-4118 (2021).
50. J. Chen, J. Qi, C. Chen, J. Chen, L. Liu, R. Gao, T. Zhang, L. Song, D. Ding, P. Zhang, and C. Liu, "Tocilizumab-Conjugated Polymer Nanoparticles for NIR-II Photoacoustic-Imaging-Guided Therapy of Rheumatoid Arthritis," Adv Mater **32**, e2003399 (2020).
51. V. Bhandari, C. Hoey, L. Y. Liu, E. Lalonde, J. Ray, J. Livingstone, R. Lesurf, Y. J. Shiah, T. Vujcic, X. Huang, S. M. G. Espiritu, L. E. Heisler, F. Yousif, V. Huang, T. N. Yamaguchi, C. Q. Yao, V. Y. Sabelnykova, M. Fraser, M. L. K. Chua, T. van der Kwast, S. K. Liu, P. C. Boutros, and R. G. Bristow, "Molecular landmarks of tumor hypoxia across cancer types," Nat Genet **51**, 308-318 (2019).
52. Q. Chen, J. Chen, M. He, Y. Bai, H. Yan, N. Zeng, F. Liu, S. Wen, L. Song, Z. Sheng, C. Liu, and C. Fang, "Novel small molecular dye-loaded lipid nanoparticles with efficient near-infrared-II absorption for photoacoustic imaging and photothermal therapy of hepatocellular carcinoma," Biomater Sci **7**, 3165-3177 (2019).